

Cosmic Shear Analysis with CFHTLS Deep data^{*}

E. Semboloni¹, Y. Mellier^{1,2}, L. van Waerbeke³, H. Hoekstra⁴, I. Tereno^{1,6}, K. Benabed^{1,2}, S. Gwyn⁴, L. Fu¹, M.J. Hudson⁷, R. Maoli^{1,5}, L. Parker⁷

¹ Institut d'Astrophysique de Paris, UMR7095 CNRS, Université Pierre & Marie Curie, 98 bis boulevard Arago, 75014 Paris, France

² Observatoire de Paris. LERMA. 61, avenue de l'Observatoire. 75014 Paris, France.

³ University of British Columbia, Department of Physics and Astronomy, 6224 Agricultural Road, Vancouver, B.C. V6T 1Z1, Canada.

⁴ Department of Physics and Astronomy. University of Victoria. Victoria, B.C. V8P 5C2, Canada.

⁵ Department of Physics. University La Sapienza. Pl. A. Moro 2, 00185, Roma, Italy.

⁶ Departamento de Física. Universidade de Lisboa, 1749-016 Lisboa, Portugal.

⁷ Department of Physics. University of Waterloo, Waterloo ON N2L 3G1, Canada.

the date of receipt and acceptance should be inserted later

Abstract. We present the first cosmic shear measurements obtained from the T0001 release of the Canada-France-Hawaii Telescope Legacy Survey. The data set covers three uncorrelated patches (D1, D3 and D4) of one square degree each observed in u^* , g' , r' , i' and z' bands, out to $i = 25.5$. The depth and the multicolored observations done in deep fields enable several data quality controls. The lensing signal is detected in both r' and i' bands and shows similar amplitude and slope in both filters. B-modes are found to be statistically zero at all scales. Using multi-color information, we derived a photometric redshift for each galaxy and separate the sample into medium and high- z galaxies. A stronger shear signal is detected from the high- z subsample than from the low- z subsample, as expected from weak lensing tomography. While further work is needed to model the effects of errors in the photometric redshifts, this results suggests that it will be possible to obtain constraints on the growth of dark matter fluctuations with lensing wide field surveys. The various quality tests and analysis discussed in this work demonstrate that MEGAPRIME/MEGACAM instrument produces excellent quality data. The combined Deep and Wide surveys give $\sigma_8 = 0.88 \pm 0.07$ assuming the Peacock & Dodds non-linear scheme (P&D), and $\sigma_8 = 0.85 \pm 0.07$ for the halo fitting model and $\Omega_m = 0.3$. We assumed a Cold Dark Matter model with flat geometry. Systematics, Hubble constant and redshift uncertainties have been marginalized over. Using only data from the Deep survey, the 1σ upper bound for w_0 , the constant equation of state parameter is $w_0 < -0.32$.

Key words. Cosmology: theory, dark matter, gravitational lenses, large-scale structure of the universe

1. Introduction

Cosmological weak lensing, also called cosmic shear, can be used to probe the dark matter distribution in the universe. Weak lensing observations complement other probes such CMB anisotropies (Spergel et al. 2003),

Send offprint requests to: sembolon@iap.fr

^{*} Based on observations obtained with MEGAPRIME/MEGACAM, a joint project of CFHT and CEA/DAPNIA, at the Canada-France-Hawaii Telescope (CFHT) which is operated by the National Research Council (NRC) of Canada, the Institut National des Science de l'Univers of the Centre National de la Recherche Scientifique (CNRS) of France, and the University of Hawaii. This work is based in part on data products produced at TERAPIX and the Canadian Astronomy Data Centre as part of the Canada-France-Hawaii Telescope Legacy Survey, a collaborative project of NRC and CNRS.

type Ia supernovae (Riess et al. 2004, Riess et al. 1998, Perlmutter et al. 1999), and galaxy redshifts (Lahav & Suto 2004). Weak lensing has also the nice feature of being free of any assumption regarding the light versus matter distributions (Mellier 1999, Bartelmann & Schneider 2001, Van Waerbeke & Mellier 2003, Réfrégier 2003).

Only recently it has been shown that cosmic shear measurement is technically feasible (Bacon, Réfrégier & Ellis 2000, Kaiser et al. 2000, Van Waerbeke et al. 2000, Wittman et al. 2000). Unfortunately, the deepest weak lensing survey has a sky coverage limited to less than one deg^2 and the widest to $\sim 10 \text{ deg}^2$. Moreover, most surveys were performed in one color only, and even rough redshift information was not available. These limitations restricted the use of weak lensing as a cosmological probe to a very

small number of parameters. Early weak lensing surveys were primarily focused on the measurements of the normalization of the dark matter power spectrum, σ_8 , and the mass density parameter, Ω_m . The most recent cosmic shear surveys reach a relative accuracy of about 10% on $\Omega_m \sigma_8^{0.5}$ (Mellier 1999, Bartelmann & Schneider 2001, Van Waerbeke & Mellier 2003, Réfrégier 2003), but the uncertainty on other parameters is still fairly large.

Second generation cosmic shear surveys are now under way in order to provide the community with multi-color data of excellent image quality, over a wider field of view. The Canada-France-Hawaii Telescope Legacy Survey (CFHTLS)¹, using the recently built MEGAPRIME/MEGACAM wide field camera, belongs to this generation. The *CFHTLS-Wide* survey (the core of the CFHTLS cosmic shear survey) will provide a large sky coverage of 170 sq.deg., and the deep four sq.deg. *CFHTLS-Deep* will provide shear information on smaller scales and as a function of look backtime, out to higher redshift than the *CFHTLS-Wide*.

Both surveys will ultimately consists of complete and homogeneous panchromatic data in u^*, g', r', i', z' . The CFHTLS observations started June 1st, 2003. Over the observing periods between June 1st 2003 and July 22, 2004, most data were taken as preliminary survey to provide detailed quality assessments and propose technical or operational improvements, when necessary. The CFHTLS-Wide has the same depth as VIRMOS-Descart, but so far, the available data is only in one color and covers ≈ 20 sq.deg.. A cosmic shear analysis with the wide data is performed in Hoekstra et al. (2005). The CFHTLS-Deep as been observed in all five filters, therefore photometric redshift are available, and will be used in this work. Moreover, the CFHTLS D1 Deep field is located in the VIRMOS-VLT Deep Survey (VVDS) F02 field which has several thousand of galaxy redshifts (Le Fèvre et al 2005) and near infrared data (on a tiny area). A combination of large and small scales from the wide and the deep data will ultimately provide an excellent data set to probe the nature of dark energy in the universe (Cooray & Huterer 1999, Benabed & Bernardeau 2001, Linder & Jenkins 2003, Benabed & van Waerbeke 2004, Jarvis et al 2005). In this work, we describe the first CFHTLS cosmic shear studies based on deep data, and then combine the Wide and Deep data analysis to derive constraints on Ω_m and σ_8 .

This paper is organized as follows: in section 2 we introduce the notations and we define the quantities we use. The data set is described in Section 3. In section 4 and 5 we present results and residual systematics and we discuss them. Conclusions and perspectives are outlined in Section 6.

2. Theoretical background

Detailed calculations and physical motivations of current weak lensing approximations have already been derived and discussed in several papers (e.g. Bartelmann & Schneider 2001). Following Hoekstra 2004, Van Waerbeke et al. 2002, Van Waerbeke, Mellier & Hoekstra 2005 we keep the same notations as in Schneider et al. 1998.

We introduce the power spectrum of the convergence k as :

$$P_\kappa(k) = \frac{9}{4} \Omega_0^2 \int_0^{\chi^H} \frac{d\chi}{a^2(\chi)} P_{3D} \left(\frac{k}{f_K(\chi)}; \chi \right) \times \left[\int_\chi^{\chi^H} d\chi' n(\chi') \frac{f_K(\chi' - \chi)}{f_K(\chi')} \right]^2, \quad (1)$$

where $f_K(\chi)$ is the comoving angular diameter distance to radial distance $\chi(z)$, and $n(\chi)$ is the redshift distribution of the sources. $P_{3D} \left(\frac{k}{f_K(\chi)}, \chi \right)$ is the 3-dimensional mass power spectrum, and κ is a 2-dimensional wave vector perpendicular to the line-of-sight.

Cosmic shear can be measured from three types of 2-point statistics, which differ only by their filtering schemes. Their wavelength sensitivity to the power spectrum and their behavior with respect to systematics are therefore different, enabling multiple cross-checked solutions. Two-point statistics are measured as a function of scale θ_c , which could either be a galaxy pair separation or smoothing window radius. The relation between each two-point statistics and the power spectrum of the gravitational convergence (*i.e.* the projected dark matter power spectrum) can be expressed as follows:

– Top hat variance:

$$\langle \gamma^2 \rangle_{\theta_c} = \frac{2}{\pi \theta_c^2} \int_0^\infty \frac{dk}{k} P_\kappa(k) [J_1(k\theta_c)]^2. \quad (2)$$

– Shear correlation function:

$$\langle \xi \rangle_{\theta_c} = \frac{1}{2\pi} \int_0^\infty dk k P_\kappa(k) J_0(k\theta_c). \quad (3)$$

– Aperture mass variance:

$$\langle M_{\text{ap}}^2 \rangle_{\theta_c} = \frac{288}{\pi \theta_c^4} \int_0^\infty \frac{dk}{k^3} P_\kappa(k) [J_4(k\theta_c)]^2, \quad (4)$$

with the aperture mass variance defined as:

$$M_{\text{ap}}(\theta_c) = \int_{\theta < \theta_c} d^2\theta \kappa(\theta) U(\theta). \quad (5)$$

where $U(\theta)$ is a compensated filter such as:

$$U(\theta) = \frac{9}{\pi \theta_c^2} \left(1 - \frac{\theta^2}{\theta_c^2} \right) \left(\frac{1}{3} - \frac{\theta^2}{\theta_c^2} \right). \quad (6)$$

¹ <http://www.cfht.hawaii.edu/Science/CFHLS/>

M_{ap} can be expressed in terms of the tangential shear component inside a circle as follows (Kaiser et al. 1994, Schneider 1996) :

$$M_{\text{ap}}(\theta_c) = \int_{\theta < \theta_c} d^2\theta \gamma_t(\theta) Q(\theta), \quad (7)$$

where the tangential shear component $\gamma_t(\theta)$ at the position θ is given by:

$$\gamma_t(\theta) = -\mathcal{R}e(\gamma(\theta)) e^{-2i\phi} \quad (8)$$

The aperture mass statistic is sensitive to curl-free correlations (E modes) generated by the (scalar) gravitational potential. Curl correlations (B modes) are then easily derived using the same statistics, after rotating each galaxy by 45 deg. If only signal present is due to lensing, then B modes should be zero at all scales, so this simple procedure is a powerful tool to asses systematic residuals in cosmic shear signal (Pen, van Waerbeke & Mellier 2002).

Unfortunately, the M_{ap} statistic is sensitive to the smallest accessible angular scales, where cosmic shear signal depends on the poorly-known non-linear evolution of the dark matter power spectrum. This shortcoming forces us to compute E and B modes on larger angular scales in a different way. For this we use the top hat shear variance and the shear correlation functions. These functions are usually derived from the ξ_+ and ξ_- shear correlation functions:

$$\begin{aligned} \xi_+(r) &= \langle \gamma_t(\theta)\gamma_t(\theta+r) \rangle + \langle \gamma_r(\theta)\gamma_r(\theta+r) \rangle, \\ \xi_-(r) &= \langle \gamma_t(\theta)\gamma_t(\theta+r) \rangle - \langle \gamma_r(\theta)\gamma_r(\theta+r) \rangle, \end{aligned} \quad (9)$$

where γ_t and γ_r are the tangential and radial projections of the shear on the local frame joining two galaxies separated by a distance r . Following Crittenden et al. 2001a, we define

$$\xi'(r) = \xi_-(r) + 4 \int_r^\infty \frac{dr'}{r'} \xi_-(r') - 12r^2 \int_r^\infty \frac{dr'}{r'^3} \xi_-(r'). \quad (10)$$

The E and B shear correlation functions are given by

$$\xi^E(r) = \frac{\xi_+(r) + \xi'(r)}{2} \quad \xi^B(r) = \frac{\xi_+(r) - \xi'(r)}{2}. \quad (11)$$

A similar relation can be found for the aperture mass and the top-hat statistics as showed in Crittenden et al. 2001b. Crittenden et al. 2001b also pointed out ξ^E and ξ^B can only be derived up to an integration constant which depends on the extrapolated signal outside the measurement range.

Finally, the amplitude of the lensing signal depends on the galaxy redshift distribution $n(w)$ (see Eq.(1)). As in previous works (see Van Waerbeke et al. 2002, Van Waerbeke, Mellier & Hoekstra 2005), we use the following redshift distribution

$$n(z) = \frac{\beta}{z_s \Gamma\left(\frac{1+\alpha}{\beta}\right)} \left(\frac{z}{z_s}\right)^\alpha \exp\left[-\left(\frac{z}{z_s}\right)^\beta\right], \quad (12)$$

where α , β and z_s parameters are derived from deep photometric redshift catalogues. The lensing signal can be predicted for any redshift range using Eq.(1) and Eq.(12).

3. The Deep CFHTLS T0001 data set

The Deep CFHTLS data used in this work consist of u^* , g' , r' , i' and z' stacked MEGACAM images that form the first CFHTLS release (hereafter T0001). The release is composed of stacked images, catalogues and relevant meta-data produced from observations in four uncorrelated fields that were carried out at CFHT with the MEGAPRIME instrument between June 1st 2003 and July 22, 2004. Details regarding each field are listed on the CFHTLS web pages².

Each MEGACAM image consists of an array of 9×4 EEV CCDs of 2048×4612 pixels each (Boulade et al 2003). The pixel scale is $0.186''$ and the camera covers a total field of $1 \text{ degree} \times 1 \text{ degree}$. The mosaic is composed of four rows of CCDs forming two 9×2 sub-mosaics stuck together. The gap left for connectors between the two rows composing each sub-mosaic is 82 arc-second. In order to produce compact deep fields, gaps have been filled by organizing observations in a series of exposure sequences with large offsets. It results in an heterogeneous pixel illumination at the borders of each CCD. This spatial flux variation induces a varying pixel signal-to-noise ratio that is taken into account by using pixel weight maps together with hand-made masks (see Section 4) to discard useless areas of each field.

Only MEGACAM images with seeing better than $1.0''$ ³ and airmass below 1.4 have been selected. However, because u^* -band data were less numerous than for other filters, we relaxed the selection criteria for this filter and kept all u^* images with seeing below $1.4''$. Only three deep fields have been selected for cosmic shear studies. The D2 deep field has been dropped from our sample because it is significantly shallower than the other three fields.

Data were calibrated and processed at CFHT and the TERAPIX data center. The full T0001 release is archived at CADC⁴ and available to any CFHTLS registered user. A description of the data processing pipeline used to produce the deep T0001 stacks is beyond the scope of the paper. The details of the T0001 stacks are given on the TERAPIX web pages⁵. Photometric and astrometric methods and quality assessments done on these data are explained in

² <http://www.cfht.hawaii.edu/Science/CFHTLS/cfhtlsdeepwidefields.html>

³ We use the seeing definition of TERAPIX releases as twice the median flux radius of a selection of point sources on each CCD. FLUX_RADIUS as measured by SExtractor, is the radius of the disk that contains 50% of the total flux. For a Gaussian profile the SExtractor seeing is almost equal to the Full Width at Half Maximum (FWHM). For a typical MEGACAM PSF, it is slightly larger (10%) than the true PSF FWHM.

⁴ <http://cadwww.dao.nrc.ca/cfht/cfhtls/>

⁵ http://terapix.iap.fr/article.php?id_article=382

a short explanatory supplement⁶. The processing (astrometric and photometric calibrations, pixel re sampling, image warping and stacking, catalogue production) uses the current first generation TERAPIX software tools and closely follows the one used for the VIRMOS-Descart survey that is described in McCracken et al 2003. We refer to this paper, and to the TERAPIX and CFHT⁷ web pages for further details.

The accuracy of the photometric calibrations can be estimated from the stellar color-color plots and the galaxy counts in all bands given on the TERAPIX T0001 pages and is also discussed in the more detailed stellar analysis done by Schulteiss et al (in preparation). In all bands, the cumulative internal and systematic photometric errors are 0.05 mag up to AB=22.5, and never larger than 0.1 to the 80% completeness limit (\approx AB=25.5). This uncertainty is sufficient for the cosmic shear studies on this paper.

Table 1 summarizes the T0001 stacks used in this work. The completeness limits have been computed by adding randomly simulated stars (Moffat profiles) inside a 2000×2000 area of each Deep field and by running the detection and photometry again, using the MAG_AUTO magnitude of SExtractor⁸ software (Bertin & Arnouts 1996). It was also checked using galaxy counts⁹. The D4- z' data have not been released by TERAPIX because the astrometric internal accuracy was below the scientific requirements. The large rms error found on D4- z' data has not been fully understood, but it results in a large number of galaxy mismatches during the u^*, g', r', i', z' catalogue cross-identification that hamper reliable panchromatic studies for many galaxies detected in this field. A more detailed investigation reveals that the D4- i' astrometric solution is also slightly altered, while data quality in other filters are excellent. Although it has no impact on the D4- u^*, g', r', i' photometric studies, a quick weak lensing analysis of the D4- i' field shows it has more systematics residuals than D1- i' and D3- i' . In contrast, the three Deep r' band data have similar quality and do not show systematics residual differences. We therefore used the r' band as the reference data sets for all comparison between the fields, and only kept the deep D1/D3 i' band data for color comparisons, when needed.

4. Detection of the shear signal

4.1. Galaxy shape parameters

Catalogues and shape measurements of galaxies are produced using the IMCAT software (Kaiser et al. 1995, hereafter KB). For each object the centroid position and the

half-light radius r_h are measured. These parameters are then used to derive orientations and raw ellipticities of galaxies from the weighted second moments I_{ij} of the galaxy light distribution. In order to minimize the noise contribution each moment is filtered using a Gaussian filter $W(\theta)$ of size r_h :

$$I_{ij} = \int d^2\theta W(\theta) \theta_i \theta_j(\theta) f(\theta), \quad (13)$$

where $f(\theta)$ is the surface brightness.

The raw ellipticity is given by:

$$\mathbf{e} = \left(\frac{I_{11} - I_{22}}{\mathcal{T}r(I)}; \frac{2I_{22}}{\mathcal{T}r(I)} \right). \quad (14)$$

where $\mathcal{T}r(I)$ represents the trace of the matrix I . We use the KSB method to get an unbiased estimator of the shear γ . This method has been tested by several teams that demonstrated it provides robust and reliable shear measurements from ground based data (see the comprehensive critical investigation of KSB and other techniques by Heymans et al 2005b, and also references therein).

4.1.1. PSF correction: the principle

Let us assume the shear-free intrinsic ellipticity of a galaxy is \mathbf{e}^0 . On the detector, its shape is eventually modified by the distortions produced by gravitational lensing effects and systematics that increase the smearing and the anisotropic component of the PSF (atmosphere, optical aberrations). Assuming these distortions are small, Kaiser et al. 1995 demonstrated the observed ellipticity, \mathbf{e}^{obs} , can be written:

$$\mathbf{e}_\alpha^{obs} = \mathbf{e}_\alpha^0 + P_{\alpha\beta}^{sh}\gamma + P_{\alpha\beta}^{sm}\mathbf{q}, \quad (15)$$

where \mathbf{q} is the anisotropic component of the PSF and γ is the gravitational shear. P^{sh} and P^{sm} are called the shear and the smear polarisability. Their values depend on the galaxy surface brightness and on the filter properties $W(\theta)$. \mathbf{q} can be derived directly from the data, by measuring the ellipticity of stars in each field, \mathbf{e}_\star , such as:

$$\mathbf{q}_\alpha = \frac{\mathbf{e}_\alpha^\star}{P_{\beta\beta}^{sm}}. \quad (16)$$

The shear polarisability is however altered by the isotropic smearing component of the PSF. It results in a modification of the shear polarisability

$$P^\gamma = P^{sh} - \frac{P_\star^{sh}}{P_\star^{sm}} P^{sm}, \quad (17)$$

where P^γ is called pre-seeing shear polarisability and $P_\star^{sh/sm}$ refers to stars (Luppino & Kaiser 1997). Provided the assumption $\langle e_0 \rangle = 0$ is valid, an unbiased estimator of the shear γ is given by:

$$\gamma = \langle P_\gamma^{-1}(\mathbf{e}^{obs} - P^{sm}\mathbf{q}) \rangle, \quad (18)$$

⁶ http://terapix.iap.fr/article.php?id_article=383

⁷ <http://www.cfht.hawaii.edu/Science/CFHTLS-DATA/dataprocessing.html>

⁸ http://terapix.iap.fr/rubrique.php?id_rubrique=91

⁹ see <http://clix.iap.fr/T0001/Plots/>

CFHTLS_D_i_galcount_T0001.png and
<http://clix.iap.fr/T0001/Plots/>
 CFHTLS_D_r_galcount_T0001.png

Table 1. Summary table of T0001 D1, D3 and D4 deep stacks used in this work. Magnitudes are instrumental AB. Details on magnitude, aperture, seeing and completeness definitions are given in the explanatory page http://terapix.iap.fr/article.php?id_article=383

	D1	D3	D4
RA (J2000)	02:25:59	14:19:27	22:15:31
DEC (J2000)	-04:29:40	+52:40:56	-17:43:56
Effective FOV (deg ²)	0.80	0.77	0.77
Exp. time u^* (s)	10560	4620	16680
Seeing u^* (arc-sec.)	1.15	0.88	1.05
Completeness u^* 50% (mag.)	26.4	26.0	26.2
Exp. time g'	7515	8010	11250
Seeing g' (arc-sec.)	0.98	0.95	0.99
Completeness g' 50% (mag.)	26.4	26.5	26.2
Exp. time r'	17280	20820	26400
Seeing r' (arc-sec.)	0.87	0.93	0.85
Completeness r' 50% (mag.)	26.1	26.4	25.9
Exp. time i'	52000	59640	58800
Seeing i' (arc-sec.)	0.88	0.92	0.88
Completeness i' 50% (mag.)	26.1	26.2	25.8
Exp. time z'	12240	15120	-
Seeing z' (arc-sec.)	0.86	0.85	-
Completeness z' 50% (mag.)	24.5	24.6	-

4.1.2. Object selection

Prior to cosmic shear analysis, all CFHTLS images are checked by eye and masks are drawn by hand. These masks are designed to avoid elongated defects, like saturated stars, as well as large foreground galaxies with extended bright halo that may contaminate the shape of underlying faint galaxies (see Van Waerbeke et al. 2001 for details). We should emphasize that masks are *only* drawn using criteria ($z = 0$ galaxies, bright stars, CCD defects) that are not correlated with the lensing signal. In addition, we used the weight map images produced by TERAPIX for each stack to reject all pixels with a relative weight amplitude less than of 80%. This rejection step reduces significant spatial variation of the detection threshold and keeps the averaged redshift distribution of lensed galaxies stable over the field. It primarily removes from each field all CCD boundaries and is almost equivalent to single out each CCD region, as it was done earlier in VIRIOS-Descart survey. The gain in homogeneity is however preserved at the expense of the sky coverage. About 30% of the initial area is lost after the masking process.

Stars needed for the PSF correction are selected along the stellar locus of the magnitude/size diagram (Fahlman et al 1994), in a region where stars are about one magnitude fainter than the saturation level and where they cannot be confused with faint galaxies. The P_{\star}^{sm} and P_{\star}^{sh} values are derived at all MEGACAM points from a PSF mapping that samples the PSF smearing and PSF anisotropy at each selected star position and by interpolating their values between each star. This operation is done on each CCD separately, as suggested by Hoekstra 2004. The PSF is mapped using a composite model of a second

order polynomial and a rational function, $p^{\alpha}(x, y)$:

$$p^{\alpha}(x, y) = a_0 + a_1x + a_2y + a_3x^2 + a_4xy + a_5y^2 + c(x, y) \quad (19)$$

where $c(x, y)$ is the rational function chosen as:

$$c(x, y) = \frac{b_0 + b_1x + b_2y + b_3x^2 + b_4xy + b_5y^2 + b_6y^3 + b_7y^4}{1 + b_8x + b_9y} \quad (20)$$

The second order polynomial terms models the smooth low frequency PSF component, while the rational function provides a model for the high frequency PSF terms (Hoekstra 2004).

The correction is made in two steps. First, the coefficients of the rational function are determined. Since the CFHTLS deep field is much deeper than the RCS (Hoekstra et al 2002) and the VIRIOS-Descart (Van Waerbeke et al. 2000, Van Waerbeke et al. 2001) surveys, the density of selected stars is higher and we do not need to map the PSF using external stellar fields. Each field has about 100 stars per CCD, so the high frequency PSF terms can be reasonably well sampled down to 0.5 arc-minute, and all coefficients of the rational function can be constrained with enough accuracy. In a second step, the polynomial terms are determined.

We also compared the rational function solution against the second order polynomial interpolation. We found the results are not very different from our composite model, although the rational function improves the quality and stability of the PSF mapping.

Once ellipticity is corrected we keep in the sample all objects with angular size larger than the seeing disk and smaller than two arc-seconds. Following

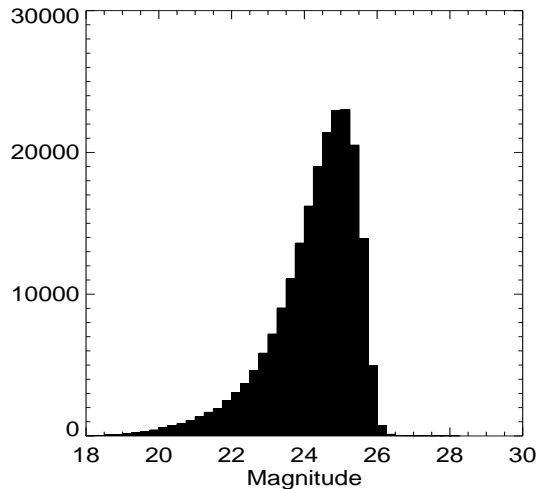


Fig. 1. Magnitude distribution of galaxies in the three fields in the r band. More detailed galaxy count plots, for each filter and for each deep field, are available in the summary table http://terapix.iap.fr/article.php?id_article=382

Van Waerbeke et al. 2000, we automatically reject one galaxy in every close pairs with angular separation less than 12 arcsec in order to avoid contamination of ellipticity measurements by overlapping isophotes of neighboring galaxies.

The magnitude distribution of the final object catalogue is shown in Fig.1. The limiting magnitude corresponding to a 80% completeness limit is $r'_{AB} = 25.5$. Bright objects with magnitude smaller than 21.5 and faint objects with magnitude larger than 25.5 are also removed from the galaxy sample. The final galaxy number density of the cosmic shear catalogue is about $20/\text{arcmin}^2$.

As proposed by Erben et al. 2001 we assign an ellipticity dispersion σ_g to each object corresponding to the ellipticity dispersion in a box containing its 20 nearest neighbors in the (*magnitude, size*) space. Weighted 2-point statistics are computed assigning to each galaxy a weight given by $1/(\sigma_g^2 + \sigma_e^2)$ where σ_e is the ellipticity dispersion of the unlensed galaxies. A different noise estimation (Hoekstra et al 2000) gives similar results.

5. Residual systematics

5.1. Quality of the PSF correction

A visual inspection of the MEGAPRIME PSF (Fig.2) shows that the PSF anisotropy has significant variation over the field and may also be very large at the boundaries¹⁰. The PSF correction is therefore a critical step and its reliability demands careful verifications. In addition to the usual B-

¹⁰ This strong PSF anisotropy has been considerably reduced by the CFHT staff, after the T0001 release. It should no longer be a critical issue for next releases.

mode analysis shown in the next section, in this section we carry out several analyses of the systematics.

The quality of the PSF correction and its homogeneity over the MEGACAM field camera can be assessed by comparing the mean star ellipticity before and after PSF correction (Fig.3). The average stellar ellipticity $\langle e_t \rangle$ and $\langle e_r \rangle$ are plotted as a function of the radial distance to the center of the field, r . It is interesting to note that the radial ellipticity component degrades much more and much faster than the tangential ellipticity. However, the PSF correction done by the PSF mapping is very good, for each deep field. After correction, the dispersion of star ellipticities is about 2×10^{-3} at any point of the camera. There is no significant change of the residual error as function of radial distance. The small increase of fluctuation observed at very small distance is due to higher Poisson noise: each radial bin has the same width, so the innermost circle encompasses the smallest area and contains fewer stars than the others.

Finally, we checked the residual amplitude of the correlation function between corrected stars. We found it to be two order of magnitude smaller than the expected lensing signal at all scales probed by this work (Fig. 4).

The tests discussed above only guarantee that the PSF correction is excellent in the neighborhood of selected stars or on angular scales larger than, or close to, the mean angular distance between stars. In regions where no stars were selected or on small scales, the local PSF correction residuals may be larger than the average. A useful test of systematic residuals on small scales has been proposed by Bacon et al. 2003 and Heymans et al 2005b. Assuming the PSF model derived from stars and applied to galaxies is unable to remove all systematic contributions, the star-galaxy cross correlation will be non-zero and may vary as function of angular scale. If the residual is small, Bacon et al. 2003 showed the systematic residual can be expressed as follows:

$$\xi_{sys} = \frac{\langle e_* e_{gal} \rangle^2}{\langle e_* e_* \rangle}; \quad (21)$$

where e_{gal} is the *corrected* galaxy ellipticity and e_* is the *uncorrected* star ellipticity. We use the ξ_{sys} to compute the contribution of systematics for both top hat and compensated filter. Fig. 5 shows they are consistent with zero at all scales between 0.5 arc-minute to 30 arc-minutes. It confirms that residual systematics are negligible on MEGACAM deep fields.

5.2. Independent analysis of r' and i' data

The robustness of cosmic shear signal can also be assessed by comparing results obtained in two different filters on the same galaxy sample. Because gravitational lensing is achromatic, we expect the shape and amplitude of cosmic shear to be identical in different colors. Any significant difference between two bands provides a useful information on the reliability of the PSF corrections. A first attempt of multi-color shear measurement was done in

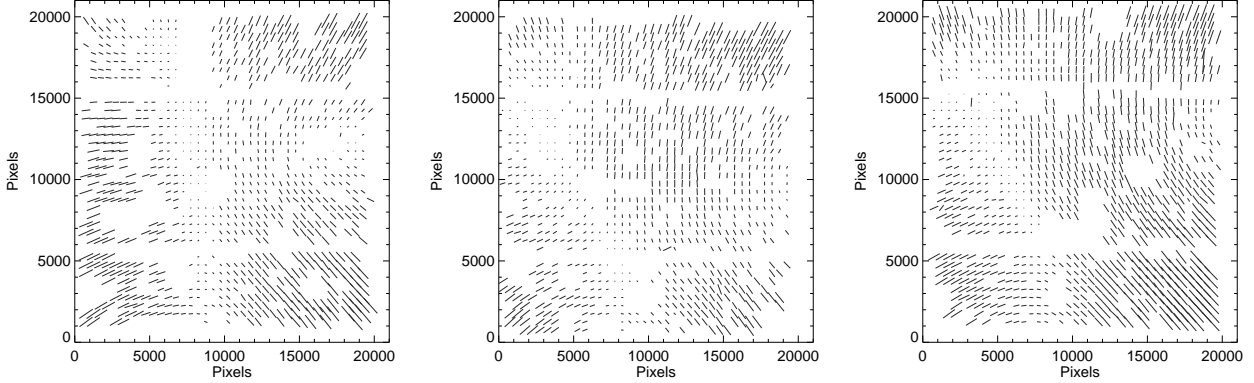


Fig. 2. PSF anisotropy maps for the three fields D1 D3 and D4 .

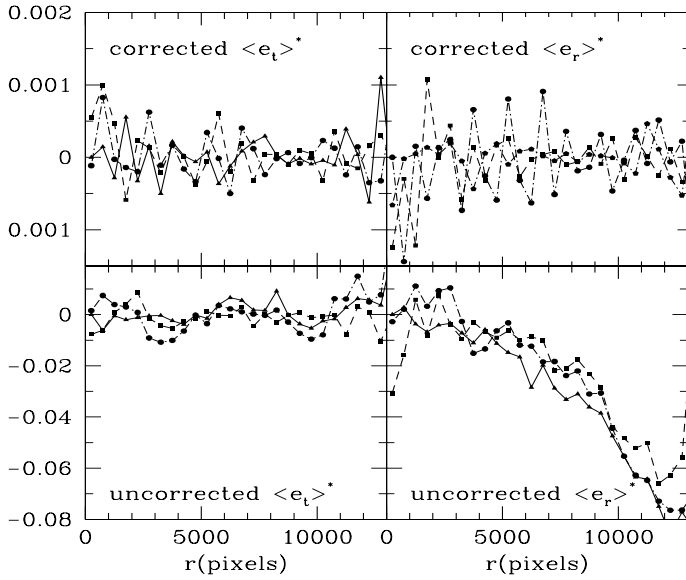


Fig. 3. Bottom panels show the mean tangential (left panel) and radial (right panel) uncorrected stellar ellipticity as a function of the distance to the center of the camera for D1rT001 (filled triangles), D3rT001 (filled squares) and D4rT001 (filled circles) fields. Top panels show the same quantities after PSF correction.

Kaiser et al. 2000 using the CFHT12K camera. The I and V bands showed significant different signals which was not consistent a change in redshift distribution between the two bands.

The CFHTLS-Deep provides a useful sample of the same galaxies detected in different filters so the expected signal is the same. However, these filters have different depths, and the shallowest colors do not have enough galaxies to allow a comparison of the signal between all colors using the same galaxies. This limitation mostly concerns with the u^* and g' bands. Furthermore, these bands are more sensitive to atmospheric dispersion than other filters. We expect their PSF anisotropy to be larger than for

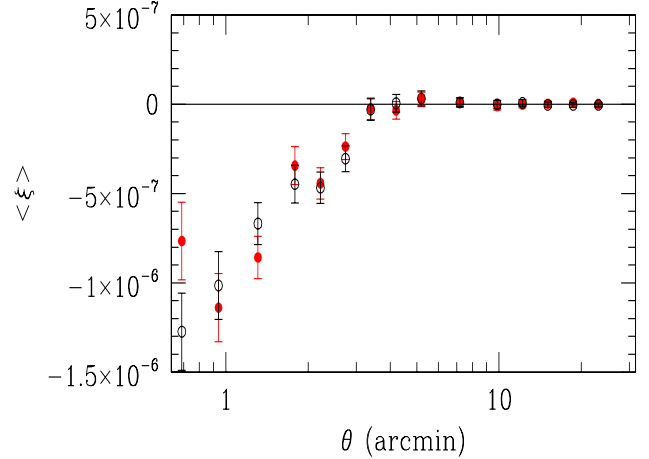


Fig. 4. E-modes (red filled circles) and B-modes (black open circles) top hat two point statistics of corrected stars show the smallness of residual PSF systematics.

r' , i' and z' bands and its correction may also depend more on the relative differences between the averaged spectral energy distributions of stars used for the PSF calibration and of galaxies. Hence, u^* and g' are not well suited for weak lensing analysis. We therefore decided only to focus on a comparison between r' and i' .

We computed the two-point statistics using the same objects in i' -band and r' -band in the D1 and D3 fields only. As reported before, D4 was discarded from this study because it shows higher systematic residuals in i' bands than the two other fields. It is worth noting that both r' and i' band images have been processed (flat fielding, astrometric and photometric calibrations, image selection, image stacking) in a totally independent way. The only correlations between the two samples are the software tools and the pipeline scheme used at TERAPIX.

The r' and i' ellipticity catalogues have been computed and PSF-corrected independently, starting from the r' and

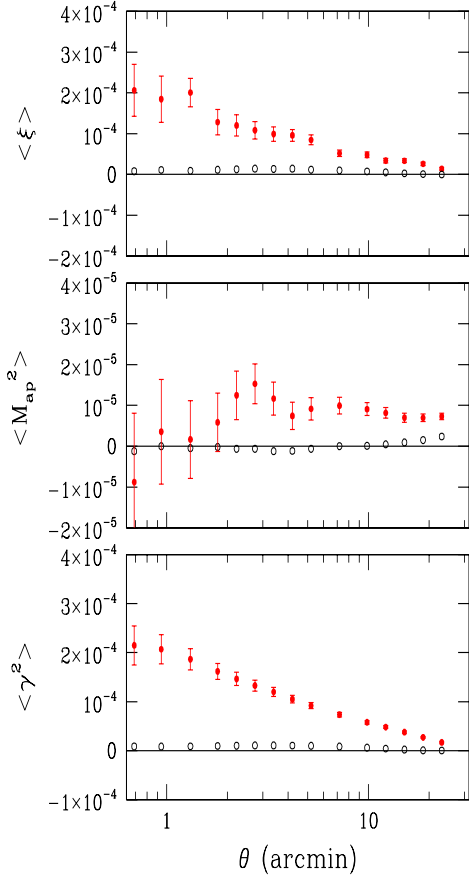


Fig. 5. Two-point signal statistics (red filled circles): top hat (bottom) and M_{ap} (middle) correlation function (top), compared with residual systematics (black open circles). Signal error bars are statistical ones.

i' T0001 stacked images. The galaxy cross-identification is done at the very end of the processing to compare the results. Fig. 6 shows the comparison of the E and B modes top-hat shear variance for both the i' and r' data sets. The error bars are estimated as the quadrature sum of the statistical and the systematic error ξ_{sys} defined by Eq.(21). The amplitude of the latter is bigger in the r' band as shown by the residual B modes in this filter. The r' and i' bands results are remarkably similar, both in shape and amplitude, they agree to within 1σ at all scales.

6. Characterization of the shear signal

6.1. Two point statistics

The ellipticity correlation functions $\xi_+(r)$ and $\xi_-(r)$ are measured from the weighted mean of all pairs with angular separation r .

The correlation function is computed using equations (10) and (11). The M_{ap} and the top-hat statistics are also computed as a function of the correlation functions $\xi_+(r)$ and $\xi_-(r)$ following Schneider et al., 2002 and Crittenden et al. 2001b. Fig. 7 shows the two-point statis-

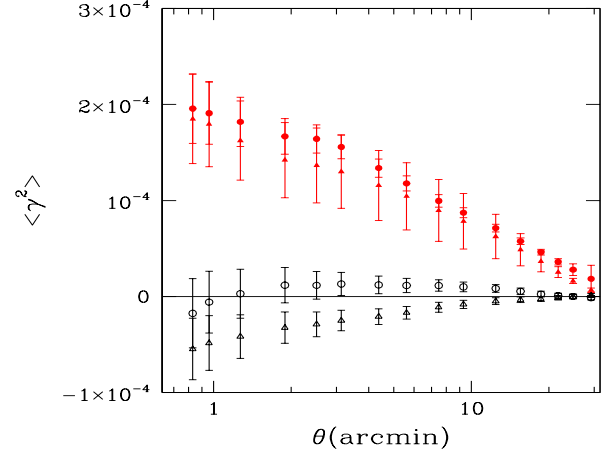


Fig. 6. Top-hat variance E modes in the I-band (red filled circles) and in the R-band (red filled triangles) for the same data set. Top-hat variance B-modes in the I-band (black open circles) and in R-band (black open triangles).

tics for the three deep fields D1, D3 and D4. Error bars including statistical noise and cosmic variance are computed from the $\xi_+(r)$ and $\xi_-(r)$ as described in Schneider et al., 2002.

The cosmic variance contribution is computed using the CFHTLS T0001 Deep survey properties: an effective¹¹ density of 19 gal/arcmin^2 an effective area of 2.1 deg^2 and an ellipticity dispersion per ellipticity component of 0.3 (the later was measured from the corrected ellipticity). However, the error calculation described in Schneider et al., 2002 is only valid for a single connected field with a density of n equally sized galaxies. We therefore replace the statistical error component by the Poisson noise measured from the data, using the weights (computed as described above) and positions of each galaxy. For the top-hat variance and the correlation function, the free integration constant is set in order to have zero B modes at scales between 15 and 25 arc-minutes. Although its amplitude is meaningless, one can see that the B-mode is flat and stable over that whole range of angular scales.

In contrast, for the M_{ap} statistics, which doesn't suffer of an undetermined integration constant (as explained previously) the B-mode amplitude is a relevant property. Fig. 7 shows the presence of B modes. A further investigation confirms that the B modes come from weak objects (i.e. $25. < mag_r < 25.5$). A magnitude cut for objects with magnitude bigger than 25. gives zero B modes at all the scales even for the M_{ap} statistics. However we keep these objects in our catalogues in the aim to have deep sample, which will be useful to study the evolution of signal with redshift. In addition the presence of B modes at small scales will taken into account at the moment of the parameters estimation (see below).

¹¹ that is after masking

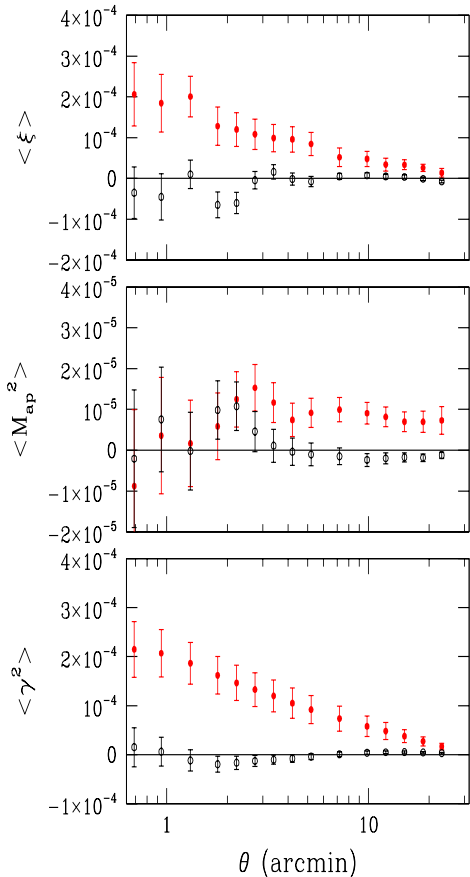


Fig. 7. Two-point statistics results for all the three field combined. Red filled circles show E-modes, black open circles show B-modes. E-modes error bars take into account the statistical error and the cosmic variance contribution, while B-modes are affected only by statistical error.

6.2. Evolution of signal with redshift

The cosmological nature of the two-point statistics signal can be established by comparing its amplitude as function of source redshifts with theoretical expectations of the gravitational instability paradigm and the gravitational lensing theory (Bernardeau et al. 1997, Jain & Seljak 1997). To first order, the signal should increase as $z^{1.5}$ (Bernardeau et al. 1997, Jain & Seljak 1997, so even a rough separation of galaxies into a low- and a high-redshift populations should split the cosmological lensing signal accordingly.

The CFHTLS T0001 data sets are well suited for this analysis. The observations can be used to sample the high redshift universe up to $z \simeq 1$. There are enough of galaxies to divide into two subsets based on their estimated photometric redshifts.

Photometric redshifts were measured using the *hyper-z* public software¹²

¹² <http://webast.ast.obs-mip.fr/hyperz/>

(Bolzonella, Miralles & Pelló 2000). *hyper-z* explores the multi-band photometric data of a galaxy to derive its most likely redshift and spectral energy distribution (SED) based on the Bruzual & Charlot evolution models (Bruzual & Charlot 1993).

We used the D1 and D3 u^* , g' , r' , i' and z' images and the D4 u^* , g' , r' , i' images (the D4- z' stacked image is missing in T0001). Photometric catalogues were produced by the *SExtractor* software. All galaxies are first detected in the r' band reference image. Magnitude and colors of galaxies are then computed using the r' -center positions and inside an aperture scaled according to the size of each galaxy in r' -band. The χ^2 minimization was performed assuming magnitude errors derived from *SExtractor*. They range between $\Delta mag = 0.03$ and $\Delta mag = 0.1$ in all bands.

Fig. 8 shows the photometric redshift distribution of the galaxies in D1 field down to $i' = 24.0$. This sub-sample can be compared with the VVDS spectroscopic redshift distribution obtained from 11000 spectra in the same region (Le Fèvre et al 2005). There are no apparent discrepancies that would make the separation into photometric low- and high-redshift galaxies unreliable. Beyond $i' = 24.$, large spectroscopic redshift samples are not yet available, but we don't have reason to believe that our photometric redshift accuracies will degrade significantly beyond $i' < 24.$ sample.

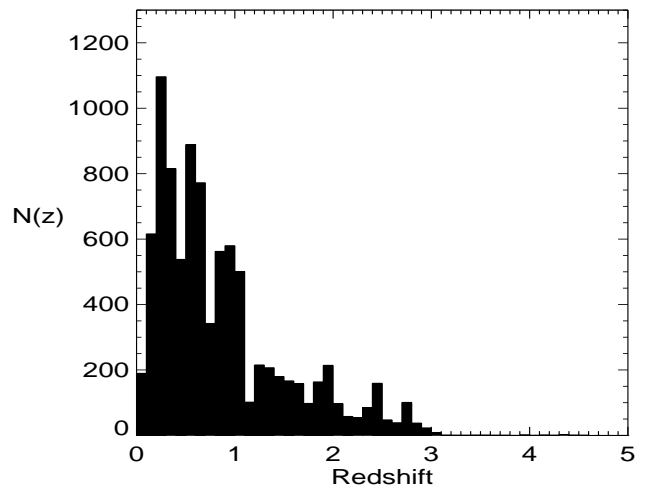


Fig. 8. Density of galaxies of D1 field as a function of photometric redshift.

The cosmic shear catalogue can therefore be split into two equally numbered samples at high and low redshifts with reasonable confidence and can be compared with cosmological predictions. Poisson noise is therefore similar in the two sub-samples, but photometric redshift errors are expected to be larger in the high-redshift tail.

Fig. 9 shows the top hat shear variance measured for the two populations. The low- z sample ranges in

Table 2. Mean photometric redshift in magnitude bins.

magnitude bin	mean redshift
$18.5 \leq i_{AB} \leq 24$	$\langle z \rangle = 0.850$
$19.0 \leq i_{AB} \leq 24$	$\langle z \rangle = 0.853$
$19.5 \leq i_{AB} \leq 24$	$\langle z \rangle = 0.858$
$20.0 \leq i_{AB} \leq 24$	$\langle z \rangle = 0.865$
$20.5 \leq i_{AB} \leq 24$	$\langle z \rangle = 0.876$
$21.0 \leq i_{AB} \leq 24$	$\langle z \rangle = 0.892$
$21.5 \leq i_{AB} \leq 24$	$\langle z \rangle = 0.913$
$22.0 \leq i_{AB} \leq 24$	$\langle z \rangle = 0.942$
$22.5 \leq i_{AB} \leq 24$	$\langle z \rangle = 0.981$
$23.0 \leq i_{AB} \leq 24$	$\langle z \rangle = 1.035$
$23.5 \leq i_{AB} \leq 24$	$\langle z \rangle = 1.100$

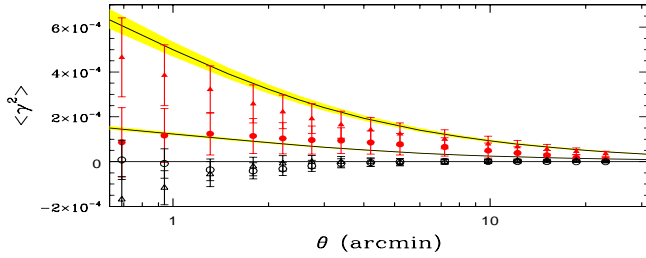


Fig. 9. Top-hat variance for “high- z ” sample (red filled triangles) and “low- z ” sample” (red filled circles). B modes concerning the two subsamples are also shown. Error bars take into account statistical noise and cosmic variance. The data are compared with theoretical fiducial model ($\Omega_m = 0.3, \Omega_\Lambda = 0.7$ and $\sigma_8 = 0.8$) and source distribution $n(z)$ modeled by Eq.12, with $\alpha = 1.98, \beta = 0.66$ and $z_s = 0.098$. The low- z source selection is simulated using $n(z)$ between $0.3 < z < 1.2$ and zero otherwise (bottom line). Likewise, the red filled triangles and the black open triangles are the E and B modes of the “high- z ” sample. The data are compared with the same theoretical model with a high- z source selection simulated using $n(z)$ between $z > 0.8$ and zero otherwise. Shaded areas show models within $z_s = 0.0981^{+0.0129}_{-0.0114}$ that represent the 1σ error region on z_s as derived from the likelihood parameter estimation.

$0.3 \lesssim z \lesssim 1.$, while the high- z galaxies have $z \gtrsim 1.0$. Error bars include Poisson noise and cosmic variance (see Sect. 4.2). The difference between the two samples demonstrates the cosmological nature of the signal.

The change in the lensing amplitude between the two galaxy populations, which is less sensitive to cosmic variance fluctuations agrees with the predictions.

An indicative comparison of signals with theoretical predictions is also plotted.

Contamination by galaxies with incorrect photometric redshift is likely important, in particular for the faintest galaxies and the high- z tail (further informations about degeneracy of photometric redshifts in the case of missing infrared bands can be found on [hyper-z](#) user’s guide).

Despite this, the cosmological imprint of large scale structures detected on the Deep CFHTLS data demonstrates MEGAPRIME is suitable for cosmic shear studies and that the CFHTLS Deep survey can probe the evolution of the dark matter power spectrum with look back time using weak lensing studies on multiple lens planes.

7. Parameter estimation

7.1. Derivation of the Likelihood function

In this Section we describe our cosmological parameter estimation. In a subsequent paper, we will perform a complete parameter estimate, combining lensing with other cosmological probes. Therefore we limit the analysis to the normalisation of the mass power spectrum (σ_8) and matter density (Ω_m) measurements. The shape parameter Γ is given by the Cold Dark Matter paradigm $\Gamma = \Omega_m h$, where $h = 0.7$ is the reduced Hubble constant. This choice of h is consistent with the Hubble Key Project. We allow the redshift of the sources to vary around the best fit which will be described in the next sub-section.

Let d_i be the input data vector (i.e. the top-hat shear variance as a function of scale θ_i), and $m_i(\Omega_m, \sigma_8, n(z))$ the prediction, function of the parameters to be estimated. The likelihood function of the data is then:

$$\mathcal{L} = \frac{1}{(2\pi)^n |\mathbf{C}|^{1/2}} \exp \left[-(d_i - m_i) \mathbf{C}^{-1} (d_i - m_i)^T \right], \quad (22)$$

where $n = 16$ is the number of angular scale bins and \mathbf{C} is the 16×16 covariance matrix,

$$C_{ij} = \langle (d_i - m_i)^T (d_j - m_j) \rangle. \quad (23)$$

\mathbf{C} can be decomposed as $\mathbf{C} = \mathbf{C}_n + \mathbf{C}_s$, where \mathbf{C}_n is the statistical noise and \mathbf{C}_s the cosmic variance covariance matrix. As we said above, the matrix \mathbf{C}_s is computed according to Schneider et al., 2002, assuming an effective survey area of the CFHTLS Deep fields: 2.1 square degrees, a number density of galaxies $n_{gal} = 23/\text{arcmin}^2$, and an intrinsic ellipticity dispersion of $\sigma_e = 0.3$ per component.

The cosmic variance is computed in the case of a Gaussian statistic. This assumption becomes inappropriate approaching on small angular scales. However on these scales, errors are still dominated by the statistical noise contribution, so the Gaussian approximation is still an excellent one (Van Waerbeke et al. 2002).

The matrix components are derived for a fiducial cosmological model corresponding to the best fit of WMAP data proposed by Spergel et al. 2003: $\Omega_M = 0.3$, $\Omega_\Lambda = 0.7$, $\sigma_8 = 0.85$, $\Gamma = 0.21$ (the reduced Hubble constant is $h=0.7$). The B mode is calibrated by marginalizing around $B = 0$ within the 1σ interval.

7.2. Parameters estimation

The source redshift distribution is calibrated to the Hubble Deep Field (HDF) catalogues, which provide a more accurate estimate of redshift in absence of infrared data in CFHTLS fields. It turns out that the F606 filter from WFPC2 is a good match to the MEGACAM r' filter. We select all galaxies with $21.5 < r' < 25.5$. The Hubble Deep Fields provide indeed high enough redshifts overlapping with the Deep fields redshift range.

We use the usual source redshift distribution model (Eq.12) and calculate a χ^2 allowing the parameter z_s to vary. We then identify the $\pm 1\sigma$ and $\pm 2\sigma$ uncertainties, which we marginalized over in the cosmological parameter estimation. We find $\alpha = 1.9833$, $\beta = 0.6651$, $z_s = 0.0981^{+0.0129+0.0209}_{-0.0114-0.0161}$. Figure 10 shows the unnormalized weight in magnitude slices in the Deep catalogues. The effect of down-weighting faint galaxies is taken into account in the source redshift estimation. Figure 11 shows the best fit model and the underlying photometric redshifts from the Hubble Deep Fields (solid line). Error bars are Poisson errors. The dashed-dotted line on Figure 11 shows the redshift distribution one would have if we ignore the weighting. The best fit redshift distribution model has a mean source redshift of ≈ 1.01 , nearly 0.2 higher in z than the Wide survey (Hoekstra et al. 2005).

The constraints on Ω_m and σ_8 are obtained after marginalization of the reduced Hubble constant $h \in [0.6, 0.8]$ and over the $\pm 2\sigma$ limits of the source redshift parameter z_s . The resulting constraints in the Ω_m σ_8 plane are given in Figure 12. This figure shows that the CFHTLS Deep field gives constraints as good as previous lensing measurements, despite its small field of view. This is the consequence of the larger fraction of high redshift galaxies, which are more strongly lensed. On the other hand, the lack of large scale measurements still hampers the degeneracy breaking between Ω_m and σ_8 . Using the Peacock & Dodds (1996) non-linear scheme, we obtain $\sigma_8 = 0.84 \pm 0.11 \pm 0.22$ ($\pm 1\sigma \pm 2\sigma$) for $\Omega_m = 0.3$. Error bars are the one and two σ errors respectively. The Smith et al. (2003) halo fitted model gives $\sigma_8 = 0.81 \pm 0.10 \pm 0.21$, which agrees with previous normalization measurements.

We then perform a measure of σ_8 by combining these constraints with those obtained on the CFHTLS Wide (see Hoekstra et al. 2005 for the details). The result is shown in Figure 13, and remarkably, the Ω_m/σ_8 degeneracy is partially broken. This is the consequence of measuring the large and small scales simultaneously as shown in Jain & Seljak 1997. For $\Omega_m = 0.3$, we get $\sigma_8 = 0.88 \pm 0.07 \pm 0.11$ using Peacock & Dodds (1996) for the

non-linear scheme and $\sigma_8 = 0.85 \pm 0.07 \pm 0.10$ for the halo fitted model (Smith et al. 2003).

The power spectrum normalization is in very good agreement with those found in medium and low source redshift surveys (Hoekstra et al 2002, Van Waerbeke & Mellier 2005). It is remarkable that the redshift distribution parameters, which have been estimated from a different survey, are such that the normalization σ_8 lies within the errors of previous measurements. This is strong evidence that deep, medium and shallow lensing surveys are in 'cosmological' agreement, hence reinforcing the ability of cosmic shear to probe the mass distribution at different redshifts and different scales.

Lensing can also be used to constrain the dark energy. Figure 14 show the upper limit on w_0 , the constant equation of state parameter derived from the Deep data only. Here we used only the Peacock & Dodds non-linear formalism (a detailed discussion on non-linear power spectrum correction in the context of Dark Energy can be found in Hoekstra et al. 2005 as well as a joint analysis of the WIDE and Deep data). We obtain $w_0 < -0.32$ at 1σ , and the contours show a strong degeneracy along the w_0 axis. This is particularly interesting because lensing combined with either cosmic microwave background (Jarvis et al. 2005) or supernovae will provide a strong constraint on the dark energy equation of state.

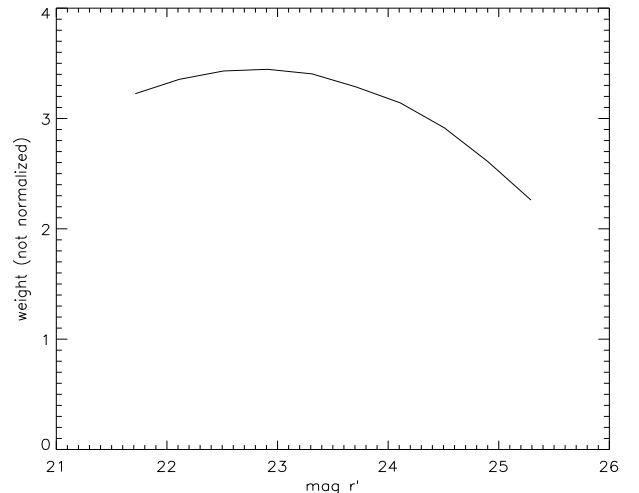


Fig. 10. Plot of mean weight per galaxy as function of magnitude $21.5 < R_{AB} < 25.5$.

8. Summary and conclusion

This paper describes the first cosmic shear studies of CFHTLS Deep data using the T0001 CFHTLS release. It uses data collected in u^* , g' , r' , i' and z' with MEGAPRIME/MEGACAM over the first year of the survey.

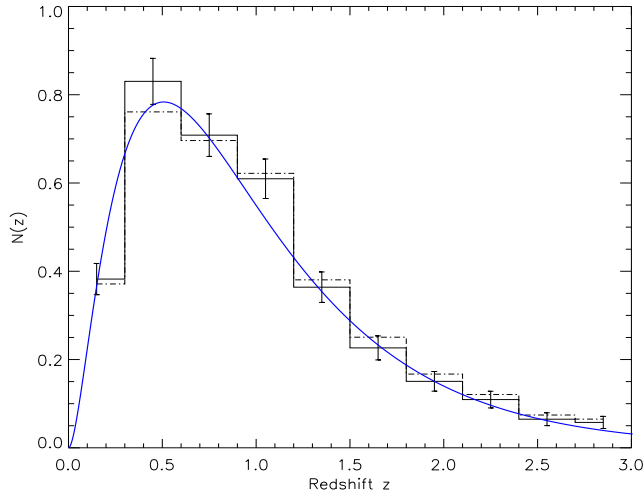


Fig. 11. The histogram shows the photometric redshift distribution of $21.5 < R_{AB} < 25.5$ galaxies of Hubble Deep Field North and South used in his work. The central solid line is the best fit model. The solid line histogram is that magnitude weighted redshift distribution. The dashed-dot histogram shows the redshift distribution if the galaxies were not magnitude weighted.

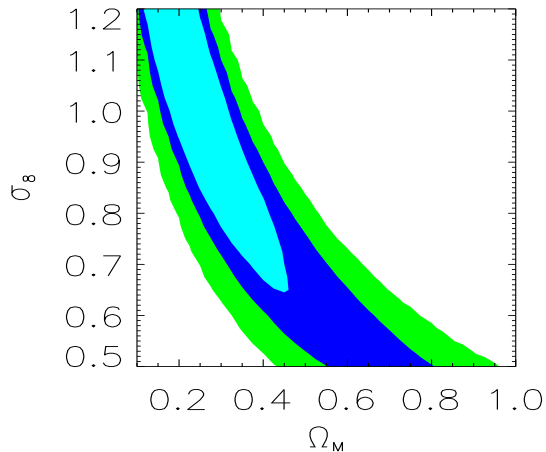


Fig. 12. Ω_m and σ_8 constraints with the Deep data only. Errors contain statistical, covariance and residual systematic contributions. The models are pure Cold Dark Matter fit to the data, marginalized over the redshift distribution (see Section 7.2 for the details).

Only 15% of the deep data are therefore in hand, and the survey is still 2-3 magnitudes below the final goal.

The T0001 data have been used to assess the capabilities of MEGAPRIME/MEGACAM and to clarify the potential and the science drivers of the CFHTLS Deep survey for weak lensing studies.

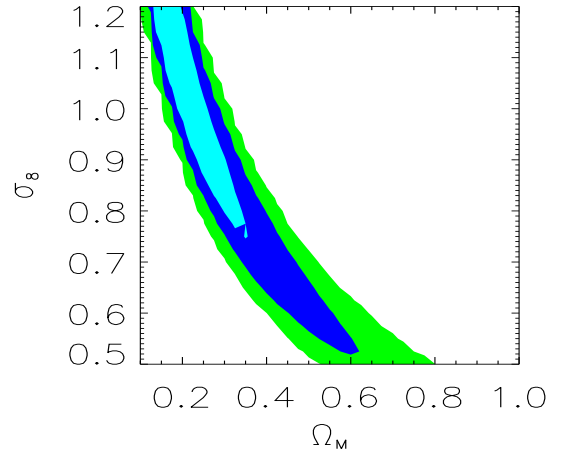


Fig. 13. Same as Figure 12, combined with the CFHTLS Wide data (Hoekstra et al. 2005). For $\Omega_m = 0.3$ we have $\sigma_8 = 0.85 \pm 0.07$ at 1σ (see Section 7.2 for details about the errors calculation).

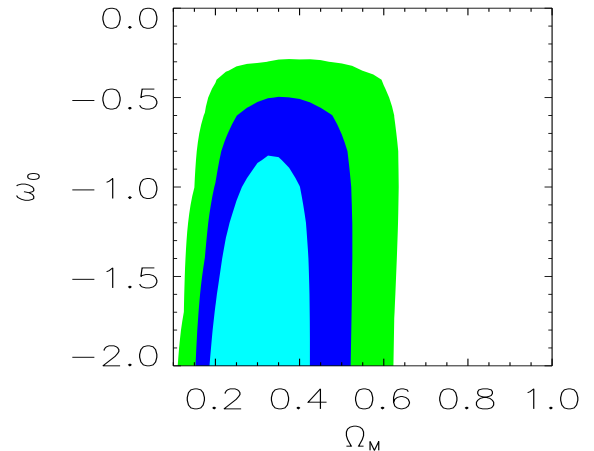


Fig. 14. Dark Energy constraints from the Deep data only. Hidden parameters are marginalized using a flat prior over $\sigma_8 \in [0.7, 1.0]$, $h \in [0.6, 0.8]$ and within the $\pm 2\sigma$ boundaries of the redshift parameter z_s (see Section 7.2).

The PSF anisotropy correction works very well on bright objects, while a further inspection is needed for weak object $25 < mag < 25.5$ which are responsible of systematics.

The cosmic shear signal has been detected in the r' band where we present results for the three standard two-point statistics. Its consistency and achromaticity has been checked by independent r' - and i' - analysis of the same data sets.

Thanks to the depth of the CFHTLS Deep sample, and using the photometric redshifts derived from the u^* , g' , r' , i' and z' images, the galaxy sample was split into low and high redshift sources. The cosmic shear signal was measured on the two samples separately. Both show zero B-modes and the shear amplitude of the high- z sample is clearly higher than the low- z one, with a ratio in agreement with the cosmic shear predictions. The amplitude of the signals are different at all scales with a significance level higher than 5-sigma and their shapes follow theoretical expectations of Λ -CDM dominated universe. This strong piece of evidence on the cosmological nature of the signal proves the CFHTLS Deep data enable to explore the growth rate of cosmic shear signal with redshift and the evolution of the dark matter power spectrum as function of look-back time.

Using only deep data and marginalising over h and the redshift of sources we derived constraints on σ_8 and Ω_m . We show that the degeneracy between these two parameters is partially broken when the analysis is combined with data coming from wide survey. Assuming $\Omega_m = 0.3$, we found $\sigma_8 = 0.88 \pm 0.07$ for P&D and $\sigma_8 = 0.85 \pm 0.07$ with the halo fitted model, in excellent agreement with Van Waerbeke, Mellier & Hoekstra 2005 ($\sigma_8 = 0.83 \pm 0.07$) and Hoekstra et al 2002 ($\sigma_8 = 0.86 \pm 0.05$). Likewise, we derive $w_0 < -0.32$ using deep data alone (see Hoekstra et al 2005 for a deep+wide analysis).

Our results show that everything is in place to make a full scientific use the CFHTLS lensing data, and that soon with the deeper Deep survey and wider Wide survey we will be able to provide the best cosmological constraints ever made with a lensing survey.

Acknowledgements. We warmly thank the CFHT, TERAPIX and CADC staff for their assistance and the considerable work they do to produce the CFHTLS data. We thank F. Bernardeau, B. Fort, C. Heymans, B. Ménard, P. Schneider, R. Pelló, C. Schimd, C. Shu, J.-P. Uzan for useful discussions. RM thanks the City of Paris and IAP for funding his research grants at IAP. YM, ES, IT and LF thanks the CNRS-INSU and the French Programme National de Cosmologie for their support to the CFHTLS cosmic shear program. ES thanks the University of British Columbia for hospitality. LF thanks the "European Association for Research in Astronomy" training site (EARA) and the European Community for the Marie Curie doctoral fellowship MEST-CT-2004-504604. LVW HH and MH are supported by the Natural Sciences and Engineering Research Council (NSERC), the Canadian Institute for Advanced Research (CIAR) and the Canadian Foundation for Innovation (CFI).

References

- Bacon, D., Réfrégier, A., Ellis, R., 2000, MNRAS 318, 625
 Bacon, D., Massey, R. J., Réfrégier, A., Ellis, R., 2003, MNRAS 344, 673
 Bartelmann, M., Schneider, P., 2001, Phys. Rep. 340, 294.
 Benabed, K., Bernardeau, F., 2001, Phys. Rev. D 64, 083501
 Benabed, K., van Waerbeke, L., 2004, Phys. Rev. D 70, 123515
 Bernardeau, F., Van Waerbeke, L., Mellier, Y., 1997, A&A 322, 1
 Bertin, E., Arnouts, S., 1996, A&A,
 Bolzonella, M., Miralles, J.-M., Pelló, R., 2000, A&A 363, 476-492
 Boulade, O., Charlot, X., Abbon, P., Aune, S., Borgeaud, P., Carton, P.-H., Carty, M., Da Costa, J. Deschamps, H., Desforge, D., Eppele, D., Gallais, P., Gosset, L., Granelli, R., Gros, M., de kat, J., Loiseau, D., Ritou, J.L., Strazynski, P., Vignal, N., Vigroux, L., 2003, SPIE 4841, 72.
 Brodwin, M., Lilly, S.J., Porciani, C., McCracken, H.J., Le Fèvre, O., Foucaud, S., Crampton, D., Mellier, Y., 2003, preprint astro-ph/0310038.
 Bruzual, G., Charlot, S. 1993. ApJ 405, 538
 Cooray, A. R., Huterer, D. 1999, ApJ 513, 95
 Crittenden, R., Natarajan, P., Pen, U., Theuns, T., 2001a, ApJ 559, 552
 Crittenden, R., Natarajan, P., Pen, U., Theuns, T., 2001b, ApJ 568, 20
 Erben, T., Van Waerbeke, L., Bertin, E., Mellier, Y., Schneider, P., 2001, MNRAS 366, 717
 Fahlman, G., Kaiser, N., Squires, G., Woods, D., 1994, ApJ 437, 56
 Heymans, C., Brown, M. L., Barden, M., Caldwell, J. A. R., Jahnke, K., Rix, H.-W. et al., 2005b, MNRAS 361, 160.
 Heymans, C., Van Waerbeke, L., Bacon, D., Bergé, J., Bernstein, G., Bertin, E., et al., 2005a, preprint astro-ph/0506112
 Hirata, C., Seljak, U., 2003, MNRAS 343, 459
 Hoekstra, H., Franx, M., Kuijken, K., 2000, ApJ 532, 88
 Hoekstra, H., Yee, H.K.C., Gladders, M.D., Barrientos, L.F., Hall, P.B., Infante, L., 2002, ApJ 572, 55
 Hoekstra, H., 2003, IAU Symposium 216, "Maps of the Cosmos", ASP Conference Series, eds. M. Colless & L. Staveley-Smith, Sydney, July 2003, preprint astro-ph/0310908
 Hoekstra, H., 2004, MNRAS 347, 1337.
 Jain, B., Seljak, U., 1997, ApJ 484, 560
 Jarvis, M., Jain, B. Bernstein, G., Dolney, D., 2005, preprint astro-ph/0502243
 Kaiser, N., Squires, G., Fahlman, G., Woods, D., 1994, in Durret, F., Mazure, A., Tran Thanh Van, J., Eds., Clusters of Galaxies. Editions Frontières. Gif-sur-Yvette, p. 269.
 Kaiser, N., Squires, G., Broadhurst, T., 1995, ApJ 449, 460
 Kaiser, N., Wilson, G., Luppino, G., 2000, preprint astro-ph/0003338
 Lahav, O., Suto, Y. 2004. *Living Reviews in Relativity*. Published by the Max Planck Institute for Gravitational Physics.
 Le Fèvre, O., Vettolani, P., Garilli, B., Tresse, L., Bottini, B., et al. 2005, A&A in press; astro-ph/0409133 .
 Linder, E. V., Jenkins, A. 2003, MNRAS 346, 583
 Luppino, G., Kaiser, N., 1997, ApJ 475, 20
 Mellier, Y., 1999. ARAA 37, 127.
 McCracken, H., Radovich, M., Bertin, E., Mellier, Y., Dantel-Fort, M., Le Fèvre, O., Cuillandre, J.-C., Gwyn, S., Foucaud, S., Zamorani, G., 2003, A&A 410, 17
 Peacock, J.A., Dodds, S.J., 1996, MNRAS 280, L9
 Pen, U.L., Van Waerbeke, L., Mellier, Y., 2002, ApJ 567, 31
 Perlmutter, S., Aldering, G., Goldhaber, G., Knop, R. A., Nugent, P., Castro, P. G., Deustua, S., Fabbro, S., Goobar, A., Groom, D. E, et al., 1999, ApJ 517, 565

- Réfrégier, A., ARAA 41, 643
- Riess, Adam G., Filippenko, Alexei V., Challis, Peter, Clocchiatti, Alejandro, Diercks, Alan, Garnavich, Peter M., Gilliland, Ron L., Hogan, Craig J., Jha, Saurabh, Kirshner, Robert P., et al., 1998, ApJ 116, 1009
- Riess, Adam G., Strolger L., Tonry J., Casertano, S., Ferguson H.C., Mobasher B., Challis P., Filippenko A.V., Jha S., Li W., Chornock R., Kirshner R.P., Leibundgut B., Dickinson M., Livio M., Giavalisco M., Steidel C. C., Benítez T., Tsvetanov, Z., 2004 ApJ 607, 687
- Schneider, P., 1996, MNRAS 283, 853
- Schneider, P., Van Waerbeke, L., Jain, B., Kruse, G., 1998, MNRAS 296, 873
- Schneider, P., van Waerbeke, L., Kilbinger, M., Mellier, Y., 2002, A&A 396, 1
- Smith, R. E., Peacock, J. A., Jenkins, A., White, S. D. M., Frenk, C. S., Pearce, F. R., Thomas, P. A., Efstathiou, G., Couchman, H. M. P., 2003, MNRAS 341, 1311
- Spergel, D. N., Verde, L., Peiris, H. V., Komatsu, E., Nolta, M. R., Bennett, C. L., Halpern, M., Hinshaw, G., Jarosik, N., Kogut, A., Limon, M., Meyer, S. S., Page, L., Tucker, G. S., Weiland, J. L., Wollack, E., Wright, E. L., 2003, ApJS 148, 175
- Van Waerbeke, L., Mellier, Y., Erben, T., Cuillandre, J.-C., Bernardeau, F., Maoli, R., Bertin, E., McCracken, H., Le Fèvre, O., Fort, B., Dantel-Fort, M., Jain, B., Schneider, P., 2000, A&A 358, 30
- Van Waerbeke, L., Mellier, Y., Radovich, M., Bertin, E., Dantel-Fort, M., McCracken, H. J., Le Fèvre, O., Foucaud, S., Cuillandre, J.-C., Erben, T., Jain, B., Schneider, P., Bernardeau, F., Fort, B., 2001, A&A 374, 757
- Van Waerbeke, L., Mellier, Y., Pelló, R., Pen, U.-L., McCracken, H. J., Jain, B., 2002, A&A 393, 369
- Van Waerbeke, L., Mellier, Y., astro-ph/0305089, Lecture given at the Aussois winter school, France, January 2003
- Van Waerbeke, L., Mellier, Y., Proceedings of the IAU Symposium 225 "Cosmological Physics with Gravitational Lensing", Y. Mellier & G. Meylan eds. Cambridge University Press 2005.
- Van Waerbeke, L., Mellier, Y., Hoekstra, H., 2005, A&A 429, 75.
- Wittman, D. M., Tyson, A. J., Kirkman, D., Dell'Antonio, I., Bernstein, G., 2000, Nature 405, 143

